Convergent extension requires adhesion-dependent biomechanical integration of cell crawling and junction contraction

Shinuo Weng, Robert J. Huebner, and John B. Wallingford*

Department of Molecular Biosciences, University of Texas at Austin

*Correspondence to:

John Wallingford
Patterson Labs
2401 Speedway
Austin, Texas
78712
Wallingford@austin.utexas.edu
512-232-2784

Abstract:

Convergent extension is an evolutionarily conserved collective cell movement that elongates the body axis of all animals and is required for the morphogenesis of several organ systems. Decades of study have revealed two distinct mechanisms of cell movement during CE, one based on cell crawling and the other on junction contraction. How these two behaviors collaborate during CE is unknown. Here, using quantitative live cell imaging we show that these two modes act both independently and in concert during CE, but that cell movement is more effective when the two modes are simultaneously integrated. Based on these findings, we developed a novel computational model that for the first time treats crawling and contraction independently. This model not only confirmed the biomechanical efficacy of integrating the two modes but also revealed for the first time how the two modes are affected by cell adhesion. Prompted by our modeling, we show that disruption of cell adhesion by knockdown of the Arvcf catenin results in specific failure of integration of crawling with contraction. These data are significant for providing new biomechanical and cell biological insights into a fundamental morphogenetic process implicated in human neural tube defects and skeletal dysplasias.

Introduction:

Convergent extension (CE) is a fundamental collective cell movement in which a developing tissue converges along one axis, thereby extending in the orthogonal direction. CE plays a crucial role during embryogenesis by shaping the body axis during gastrulation and neurulation and by elongating tubular organs during organogenesis. The cell movements of CE are evolutionarily conserved in animals ranging from nematodes and arthropods to vertebrates. Moreover, failure of CE leads to severe birth defects, including neural tube defects, heart defects, and skeletal dysplasias (Butler and Wallingford, 2017; Huebner and Wallingford, 2018; Tada and Heisenberg, 2012).

Two distinct cellular mechanisms for convergent extension have been described, and these were initially discovered in different cell types. The first was discovered by work on *Xenopus* body axis elongation during gastrulation (Keller and Hardin, 1987; Keller and Tibbetts, 1989; Shih and Keller, 1992). In this case, intercalation of mesenchymal cells is driven by polarized actin-based protrusions extending from the mediolateral (ML) vertices of cells. These resemble a combination of sheet-like lamellipodia and spike-like filopodia on the leading edge of migrating cultured cells. These protrusions form stable contacts and exert tension on neighboring cells, thus driving cell intercalation and CE in a manner similar to cell migration (**Fig. 1A, green**). The second cellular mechanism was discovered in epithelial cells during *Drosophila* germband extension (Bertet et al., 2004; Zallen and Wieschaus, 2004). In this case, cell intercalation is achieved via polarized junction remodeling, in which junctions joining anteroposterior (AP) neighbor cells shorten via actomyosin contraction (Bertet et al., 2004; Zallen and Wieschaus, 2004)(**Fig. 1A, purple**). We will refer to these two distinct modes as the “crawling” and “contraction” modes, respectively.

The two modes were initially considered as distinct mechanisms that were implemented in either mesenchyme or epithelia (e.g. (Lienkamp et al., 2012; Nishimura et al., 2012)), cell types that differ significantly in terms of cell-cell adhesion and cell polarity. However, recent evidence suggests that most cell types employ both modes during CE (Huebner and Wallingford, 2018; Shindo, 2018). For example, the two modes were found to work in conjunction in epithelial cells, first in the mouse neural plate, and later in the *Drosophila* germ band (Sun et al., 2017; Williams et al., 2014). In both cases, the crawling mode acts via basolaterally-positioned

protrusions, while contractions act apically, at the epithelial junctions. Interestingly, we previously identified a role for the contraction mode in CE of mesenchymal cells of the *Xenopus* notochord (Shindo et al., 2019; Shindo and Wallingford, 2014), the very cells in which the crawling mode was first defined. Together, these data suggest that crawling and contraction modes may be integrated in some manner to confer a maximal biomechanical advantage. The nature of such integration is entirely unknown, however.

Here, we used mosaic labelling and quantitative live-cell microscopy together with a novel computational model of convergent extension to demonstrate that cell crawling and junction contraction act both independently and collaboratively to drive CE in *Xenopus* and that integration of the two modes is both more effective and essential for normal convergent extension. Furthermore, our modeling suggest that fine control of cell adhesion is essential for normal integration of crawling and contraction, and experimental manipulation of the C-cadherin interacting catenin Arvcf *in vivo* validated this prediction. These data are significant for providing new biomechanical and cell biological insights into a fundamental morphogenetic process implicated in human neural tube defects and skeletal dysplasias.

Results & Discussion:

Analysis of biomechanical proxies suggest a complex relationship between crawling and contraction during convergent extension

We chose to study the mesenchymal cells of *Xenopus laevis*, a key paradigm for studies of the cell biology, molecular biology, and biomechanics of CE (Chu et al., 2020; Keller et al., 2003). Because cell biological studies suggest that both crawling- and contraction-based cell intercalation is active in these cells, we first asked if simple biomechanical tools may provide insights into if/how these two modes collaborate.

First, we considered the angle (ϕ) between neighboring cell junctions converging on an ML vertex (**Fig. 1a', b' red**), which we and others have used as a proxy for cortex tension imparted by junction contraction (Rauzi et al., 2008; Shindo and Wallingford, 2014). However, while ϕ correlates with cortex tension *at the population level* in laser cutting experiments, a closer examination of these data reveals a wide distribution of cortex tensions at any given angle ϕ (see (Shindo and Wallingford, 2014), suggesting that ϕ may not adequately capture the underlying biomechanics.

We therefore considered an additional biomechanical proxy, the curvature of ML junctions, κ (**Fig. 1a', b', blue**), reasoning that this value may reflect pushing on the ML vertex by a crawling cell. Simple mechanics would suggest that when crawling dominates, ϕ will increase and κ will decrease; the converse will be true when contraction dominates (**Fig. 1a', b'**). However, an analysis of image data from the *Xenopus* notochord revealed that ϕ and κ are actually rather poorly correlated (**Fig. 1C**). This result suggests previously-applied metrics for estimating biomechanical forces during CE do not provide the full picture, and moreover, that the relationship between cell crawling and junction contraction during CE is not a simple one.

Direct quantification of crawling- and contraction-based cell intercalation during convergent extension

We next sought to directly assess the contributions of cell crawling and junction contraction. To this end, we imaged explants of the *Xenopus* dorsal marginal zone ("Keller" explants) that were uniformly labelled with the membrane marker memBFP, and mosaically labelled for different colors of an actin biosensor (lifeact-RFP/lifeact-GFP)(**Supp. Fig. 1**). This approach allowed us to use the uniform membrane-BFP to segment cells and to assess cell intercalation, while simultaneously using lifeact-GFP and -RFP to unambiguously quantify actin dynamics. We used the intensity of the actin signal at ML protrusions as a metric to quantify the contribution of crawling and that at AP cell interfaces to quantify contraction (**Fig. 2A**).

Actin dynamics are known to be pulsatile in both crawling and contraction modes (Kim and Davidson, 2011; Pfister et al., 2016; Shindo et al., 2019; Shindo and Wallingford, 2014), and this property was apparent when we used kymographs to visualize actin dynamics at ML cell protrusions and AP cell interfaces (**Fig. 2B, C**). Strikingly, both ML and AP actin dynamics were highly heterogeneous and unsynchronized, though AP contraction pulses were mostly restricted to the vicinity of the tricellular vertices (**Fig. 2B**, tricellular region, TCR). Actin dynamics were less pronounced along the middle portion of AP junctions (**Fig. 2B**, Mid).

For quantification, we determined the changes in mean intensity of the distinct actin reporters labelling ML or AP cells, focusing on the region near tricellular vertices (tCR; **Fig. 2A**; **Supp. Fig. 2**). We then asked how the dynamics at each site relate to cell intercalation, quantified as the displacement of tricellular vertices determined from the uniform memBFP signal (**Fig. 2D; Supp. Fig. 2, 3**). The justifications for these chosen definitions are described in detail in the Methods section.

We considered that crawling and contraction mechanisms could either "take turns" or work together, or both. To explore these possibilities, we took advantage of the pulsatile nature of both actin dynamics and cell movement during CE. We first used individual peaks in intercalation velocity curves over time to identify single intercalation "steps" (**Fig. 2D, left**). Then, for each step, we searched for cross-correlated peaks in ML and AP actin and used their correlation to infer the driving force for each step (**Fig. 2D, right**). This method allows us to unambiguously associate cell intercalation movement with crawling- and/or contraction-related actin dynamics.

Crawling and contraction act both independently and in concert to drive CE

In our data, we could clearly identify intercalation steps driven exclusively by cell crawling (i.e. correlated with a peak in ML actin intensity)(**Fig. 2E**) or by contraction (i.e. correlated with a peak in AP actin intensity)(**Fig. 2F**). However, we also identified steps associated with peaks in both ML and AP actin intensity (**Fig. 2G**), suggesting a simultaneous integration of crawling and contraction (schematized in **Fig 2I**).

In our data, we could clearly assign a driving force to roughly 60 percent of all observed intercalation steps (**Supp. Fig. 4**). Of, these we found that roughly one third of all steps were associated purely with crawling, another third with contraction, and the final third with both (**Fig. 2H, top**). Intercalation steps are known to be highly heterogeneous, so it was notable that when we considered the duration, rather than the number of steps, we again found an equal distribution of crawling, contraction, and integrated steps (**Fig. 2H, middle**). Strikingly, however,

when we considered actual vertex displacement (i.e. the amount of cell movement), we found that integrated steps accounted for far more than one third of the distance moved by tricellular vertices (**Fig. 2H, lower**). These data affirm the complex relationship between crawling and contraction, and moreover, suggest that the two modes can be simultaneously integrated to produce more effective cell movement than can either mode acting alone (**Fig. 2I**).

Simultaneous integration of crawling and contraction improves the efficacy of cell intercalation

To better understand the impact of crawling, contraction, and integrated steps, we quantified several additional metrics. First, we found that integrated steps exhibited significantly higher displacement per step than did crawling- or contraction-only steps, as expected (**Fig. 3A**). Moreover, we found that the improved displacement was related not only to an increased duration of the step, but that the velocity of vertex movement was faster in integrated steps (**Fig. 3B, C**). Finally, we noted that some integrated steps involved not just one peak each for crawling and contraction, but rather involved multiple peaks (**Fig. 3D**). We reasoned that if integration provided better efficacy, then steps with multiple peaks should be the most productive. This was indeed the case, as intercalation steps accompanied by multiple integration events exhibited significantly more displacement and a higher velocity than did those accompanied by only a single-integration event (**Fig. 3E, F**). Thus, integration of crawling and contraction produces more effective movement by making each intercalation step both longer-lasting and faster than crawling-only or contraction-only steps.

Integration of crawling and contraction enhances actin assembly

We next sought to understand how integration produced more effective intercalation. Previous studies in *Drosophila* suggest that tension generated by actomyosin contraction in one cell can stimulate actomyosin contraction in an adherent neighboring cell (e.g. (Fernandez-Gonzalez et al., 2009; Martin et al., 2010). We therefore asked how integration impacts actin dynamics. To this end, we quantified the intensity of actin in ML protrusions during crawling-only steps and in ML protrusions during integrated steps. Strikingly, the mean ML actin intensity associated with integrated steps was significantly higher than that of similar peaks in crawling-only steps (**Fig. 4A, green**). We observed the same trend when we examined actin along AP cell interfaces (**Fig. 4A, purple**). Moreover, the duration of both ML and AP actin pulses was also longer for integrated steps (**Fig. 4B**). Thus, the more effective movement of integrated intercalations is associated with longer and stronger actin assembly at both ML crawling and AP contraction sites.

A novel vertex model recapitulates many features of integrated crawling- and contraction-based convergent extension

Theoretical modeling is a crucial tool in studies of morphogenesis, as it allows manipulation of attributes that may be difficult or impossible to manipulate experimentally, and several modeling studies have been used to explore the mechanics of convergent extension (Alt et al., 2017; Fletcher et al., 2017; Merkel and Manning, 2017). However, the vertex models commonly employed for such studies are severely limited, because *a)* they generally treat each cell-cell junction as a single homogeneous feature and *b)* they do not independently consider contributions from cell crawling and junction contraction.

To overcome these limitations, we re-envisioned the vertex model of convergent extension. We represented each cell not as a six-vertex hexagon, but instead as 90-vertex polygon, allowing us to model local events in discrete regions of the cell cortex (**Fig. 4A**). Furthermore, cell-cell junctions *in vivo* are formed of two apposed cell membranes, which though linked by cell-cell adhesion molecules, can behave independently. We therefore modeled junctions between two cells as two independent entities, connected via cell-cell adhesion (**Fig. 5B**).

Details of the model are presented in the Methods, but briefly, we invoke three key forces: The contractile force from actomyosin pulses ("M_{pulse}") for junction contraction was modeled with Hill's muscle model ("F1"); the pushing force for cell crawling was modeled as a defined force profile localized near vertices ("F2"); and the force transmitted between neighboring cells via force-dependent cell adhesion at cell interfaces (reflecting the known role of Cadherin adhesion in convergent extension (Brieher and Gumbiner, 1994; Fagotto et al., 2013; Pfister et al., 2016), was modeled as a catch-slip bond with given adhesion units ("F3", "$N_{adhesion}$")(**Fig. 5B**).

This model successfully recapitulated many gross aspects of convergent extension. In four cell models, we consistently observed not just cell intercalation, but also resolution of T1 transitions, with formation and elongation of new junctions (**Fig. 5C**). Moreover, when 22 cells were modelled, we consistently recapitulated both cell intercalation and tissue-wide convergent extension (**Fig. 5D**). Importantly, across a wide range of parameters, we consistently observed that steps in which crawling and contraction occurred simultaneously exhibited greater vertex displacement as well as increased mean vertex velocity (**Fig. 5E, F; Supp. Fig. 5**), precisely as we observed *in vivo* (**Fig. 3A, C**). Thus, our modeling of cell-autonomous cortex behaviors, cell-cell adhesion, cell crawling, and junction contraction can recapitulate both the gross and fine-scale behaviors observed in convergent extension *in vivo*.

Modeling insights into the biomechanics of crawling, contraction, and adhesion during convergent extension

To gain insights into the biomechanics of convergent extension, we next used our model to ask how relative changes in the strength of crawling or contraction events impacted discrete cell behaviors. By exploring parameter space, we observed several trends. First, we found that integration of contraction and crawling improved intercalation efficacy under all conditions, as expected (**Supp Fig. 5**). More importantly, we also found that the synergistic effects of integrated intercalation events compared to crawling-only or contraction-only events was most pronounced when contraction forces were relatively high and crawling forces were relatively low (**Fig. 5G-H**).

For example, integration increases the duration of crawling pulses *in vivo* (**Fig. 4B**), and we observed that this effect was most pronounced when values for the crawling force (F_2) were relatively low and those for the actomyosin pulses M_{pulse} were relatively high (**Fig. 5G, H**). Conversely, integration also increased the strength of contraction pulses (**Fig. 4A**), and in our model this synergy was observed as increased contraction forces ("F1") when actomyosin pulses M_{pulse} were relatively high (**Fig. 5J**). Curiously, this synergy was not sensitive to changes in crawling forces (**Fig. 5I**). These data further demonstrate the veracity of our novel modeling approach, and moreover provide biomechanical insight by suggesting that the crawling-contraction integration takes advantage of mechanosensitive responses of actomyosin dynamics to advance cell intercalation for CE.

Finally, we examined the effect of cell adhesion in our model by modulating the adhesion units available $N_{adhesion}$ while maintaining a constant, relatively high actomyosin pulses M_{pulse} and a constant crawling force F_2. We again found that the improved overall efficacy of integrated intercalation was robust across a wide range of adhesion parameters, though the overall relationships were non-linear (**Fig. 6A**). Far more striking was the effect of changing adhesion on the efficacy of non-integrated events. Indeed, low adhesion strongly favored crawling-only intercalation while severely inhibiting contraction-only intercalation (**Fig. 6A**). In addition, these changes in adhesion also impacted finer-scale behaviors. For example, the improved duration of ML actin pulses in integrated events as compared to crawling-only step was observed only with relatively higher adhesion levels (**Fig. 6B**). Conversely, the enhanced AP actin in integrated steps was more robust in lower adhesion regimes, although there is a pronounced trend for the contraction force to decrease with adhesion (**Fig. 6C**). Together, these data suggest that the proper integration of crawling and contraction, which is essential for normal cell intercalation, is highly dependent upon finely tuned cell adhesion.

The ARVCF catenin is specifically required for integration of crawling and contraction.

Finally, we sought to validate our new modeling approach by experimentally modulating parameters that reflect those in the model. However, known regulators of actomyosin during CE, such as PCP proteins or Rho family GTPases, evoke highly pleiotropic effects on subcellular behaviors during *Xenopus* CE (Goto and Keller, 2002; Kinoshita et al., 2003; Shindo and Wallingford, 2014; Wallingford et al., 2000). Likewise, disruption of cell adhesion, for example by manipulation of C-cadherin, results in similarly catastrophic defects, which could be confounding (Brieher and Gumbiner, 1994; Fagotto et al., 2013; Pfister et al., 2016).

We therefore chose to explore the function of Arvcf, a catenin protein implicated in cadherin-based adhesion and Rho GTPase regulation that is essential for convergent extension during *Xenopus* gastrulation (Fang et al., 2004; McCrea and Park, 2007). It is thought that Arvcf regulates adhesion indirectly via modulation of the cytoskeleton (Cho et al., 2010; Reintsch et al., 2008), but the basis of convergent extension defects following Arvcf loss are entirely unknown. Because Arvcf also controls convergent extension during craniofacial morphogenesis and is implicated in human disease (Cho et al., 2011; McCrea and Park, 2007; Tran et al., 2011), it represents an excellent candidate for deeper analysis using the new tools developed here.

We knocked down Arvcf using antisense morpholino-oligonucleotides that have been previously validated by rescue experiments in *Xenopus* (Fang et al., 2004; Reintsch et al., 2008; Tran et al., 2011) and performed time-lapse imaging of convergent extension in Keller explants. As expected, convergent extension was disrupted, as evidenced by a significant defect in the velocity of cell intercalation, though cell polarity was largely normal (**Fig. 7A, B**). This result suggests that the cell biological basis of the CE defect is more subtle than that associated with disruption of Planar Cell Polarity signaling or C-cadherin.

To understand this more subtle defect, we again employed our mosaic labeling approach and quantified crawling-only, contraction-only, and integrated intercalation steps. Loss of Arvcf specifically disrupted the improved efficacy of integrated intercalation steps (**Fig. 7C-E**). Thus, while the numbers and duration of crawling-only, contraction-only, or integrated steps were unchanged in morphants (**Fig. 7C, D**), the amount of displacement driven by integrated intercalation steps was significantly reduced (**Fig. 7E**).

Our modeling suggests that decreased adhesion eliminates the synergistic effect of integrated steps specifically by impacting the enhanced actin assembly on ML protrusions, but not the actin pulses on AP junctions (**Fig. 6B, C**). Consistent with the known role for Arvcf in controlling cell adhesion (Cho et al., 2010; Reintsch et al., 2008), the enhanced actin assembly normally observed in ML protrusions during integrated steps as compared to crawling-only steps was severely disrupted in Arvcf morphants (**Fig. 7F, G**). This effect was apparent in both the duration and the magnitude of these actin assembly events **(Fig. 7F, G**). By contrast, the synergistic effect of integrated steps on contraction-related actin at AP interfaces was not altered (**Fig. 7H, I**), again as predicted by our model (**Fig. 6C**). Thus, *in silico* and *in vivo* approaches suggest the precise control of cell adhesion is critical for integration of cell crawling and junction contraction during convergent extension.

Conclusions: Here we have combined live imaging and a new approach to modeling to reveal the mechanisms by which two modes of cell motility collaborate to drive a crucial morphogenetic process in early vertebrate embryos.

Our live imaging approach allowed us to isolate and quantify the actin assembly associated with crawling and contraction independently. By doing so we show that when crawling and contraction are coupled, actin assembly associated with both processes is enhanced, consistent with the mechanosensitive responses of actomyosin in other systems (e.g. (Fernandez-Gonzalez et al., 2009; Martin et al., 2010). Moreover, this more robust actin assembly in turn substantially improves the efficacy of cell intercalation. Our work in mesenchymal cells in *Xenopus* suggests that the crawling- and contraction-based intercalation mechanisms in epithelial cells (e.g. (Sun et al., 2017; Williams et al., 2014) may likewise be coupled.

In addition, our new approach to modeling of CE provides a substantial advance over previous models, as it independently captures not only junction contraction, but also cell crawling and cell-cell adhesion, as well as treats individual cell cortices independently from one another. Despite the substantial increase in the complexity of out model, it nonetheless recapitulates both gross and fine characteristics of CE as observed *in vivo*. Given the model's ability to accurately predict the effect of modulating cell adhesion on fine-scale cell behaviors that can be validated *in vivo*, we feel this model will provide a very useful resource for the community.

Finally, the work provides important new insights into the role of cell adhesion in vertebrate CE. Though studied extensive in *Drosophila* (e.g. (Levayer and Lecuit, 2013; Truong Quang et al., 2013), the role of cadherin adhesion in vertebrate gastrulation is only poorly understood. Recent suggest a key role in both crawling- and contraction-based intercalation (Huebner et al., 2020; Pfister et al., 2016), but our work here further demonstrates that fine-tuning of adhesion is crucial for the integration of the two, which is itself essential for normal morphogenesis. Further exploration of cadherin adhesion and its role in integrating biomechanical forces that drive CE will be important.

Figure 1. Biomechanical proxies suggest a complex relationship between crawling and contraction during convergent extension. (A) Sketch showing crawling mode in a 4-cell model, with actin in ML protrusions in green. (a') Crawling forces (green arrowheads) would be expected to increase the angle ϕ and generate a negative curvature κ. (B) Sketch showing contraction mode in a 4-cell model with actin at AP interfaces in purple. (A, anterior; P, posterior, ML, mediolateral). Actin in protrusions for cell crawling is colored in green and actin in cell cortex for junction contraction is colored in magenta. (a') contraction forces (purple arrowheads) would be expected to decrease the angle ϕ and generate a positive curvature κ. (C) Angle ϕ and curvature κ are poorly correlated in cells of the Xenopus DMZ, suggesting a complex relationship between crawling and contraction during cell intercalation.

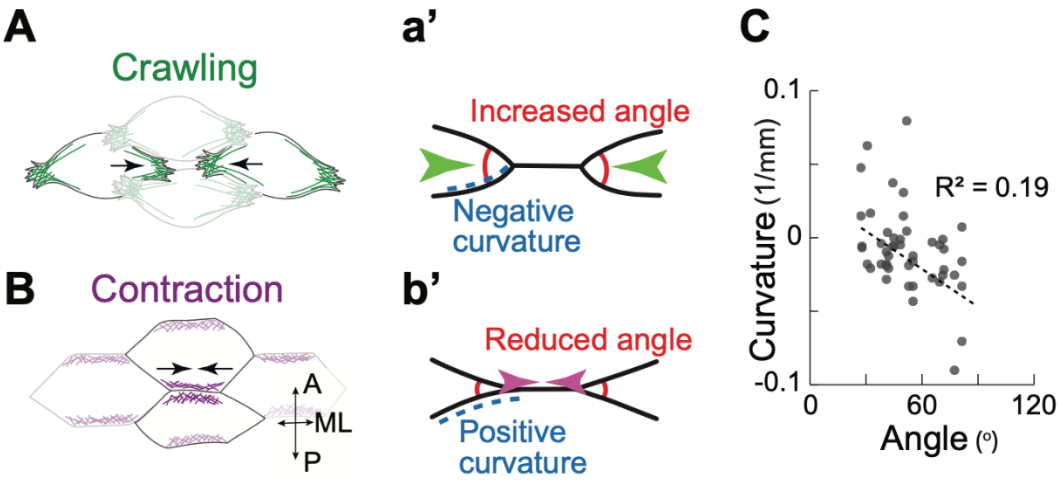

Figure 2. Direct quantification of crawling- and contraction-based cell intercalation during convergent extension. (A) Still images from a representative time-lapse movie showing membrane (blue), actin in the ML protrusions (green signal, arrowheads) and actin at AP interfaces (magenta). Boxes indicate tricellular regions (tCR) and the Mid region, see text for details. (B&C) Kymograph along the interface between AP cells in (B) shows spatiotemporal changes of actin from the ML protrusions representing the "crawling "signal (C) see shows the AP junction actin in along the same interface, the "contraction" signal. (D) Method for quantifying crawling and contraction: Left, peaks on the trace of intercalation velocity were used to identify intercalation steps. Right, for each step identified (black traces), correlated crawling (green) or contraction (purple) peaks were identified from traces of ML or AP actin intensity

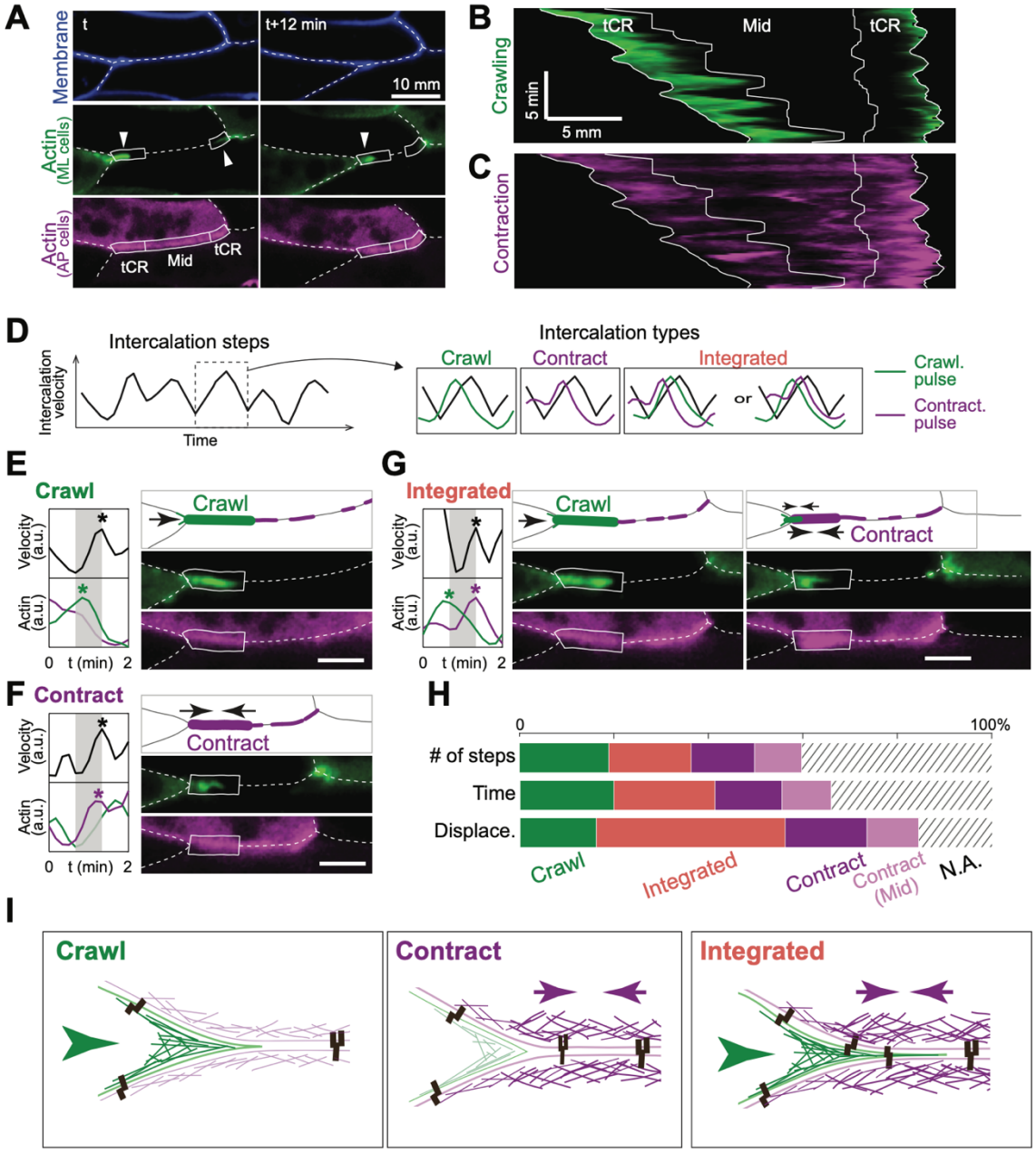

(green and purple, respectively). In some cases, a single intercalation step correlated with peaks in both crawling and contraction (far left), which we define as “integrated” steps. (E-G) Examples of crawling, contraction, and integrated steps, showing traces, a schematic, and still frames from time-lapse data. (I) Schematic showing crawling steps driven by actin in ML cells, contraction steps driving by actin in AP cells, and integrated contractions driven by both. (H) Quantification of the number, duration and cell vertex displacement for crawling, contraction, and integrated steps (note that contraction steps are separated into two group, those resulting from contraction in the tCR and those in the Mid region of the interface). Data are collected from 57 vertices involved in intercalation.

Figure 3. Simultaneous integration of crawling and contraction improves the efficacy of cell intercalation. (A) Violin plot demonstrating that integrated steps produce greater intercalation than do crawling or contraction steps. (B, C) Violin plots demonstrating that integrated steps increase both the step duration and step velocity. (D) Traces of actin intensity reveal that some integrated steps involve more than a single peak in crawling or contraction signal. (E, F) Multiple integration further improves the intercalation displacement and velocity.

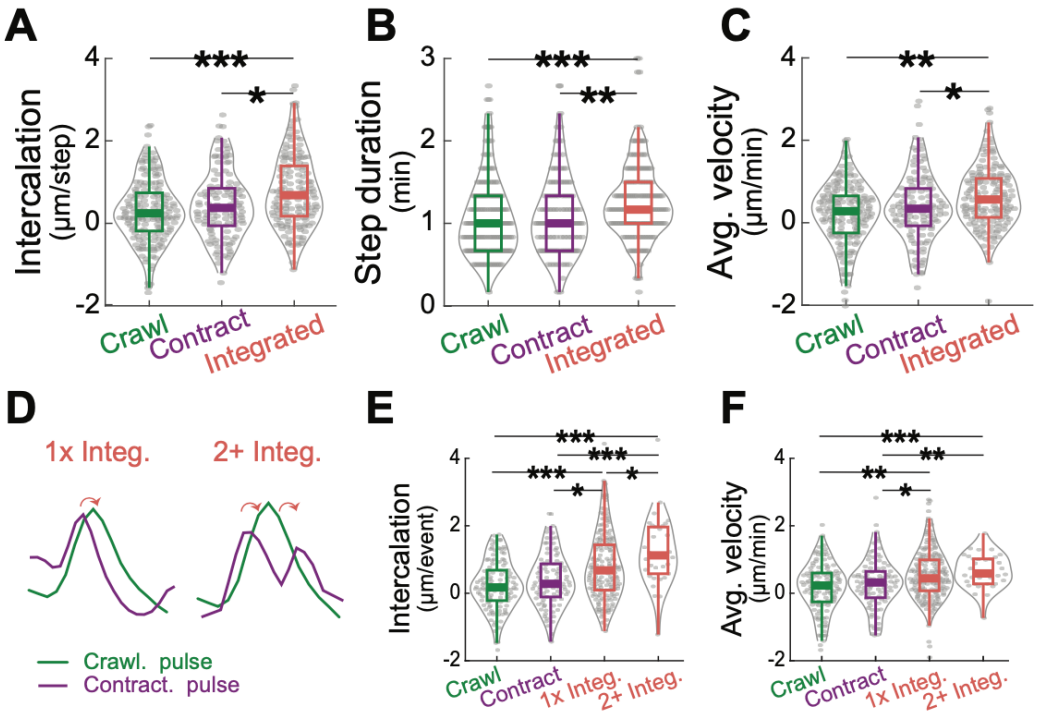

Figure 4. Integration of crawling and contraction enhances actin assembly. (A) Violin plot demonstrating that the intensity of both ML ad AP actin assembly is enhanced when crawling and contraction are integrated, as compared to crawling-only and contraction-only steps. (A) Violin plot demonstrating that the duration of ML ad AP actin assembly events is increased when crawling and contraction are integrated, as compared to crawling-only and contraction-only steps.

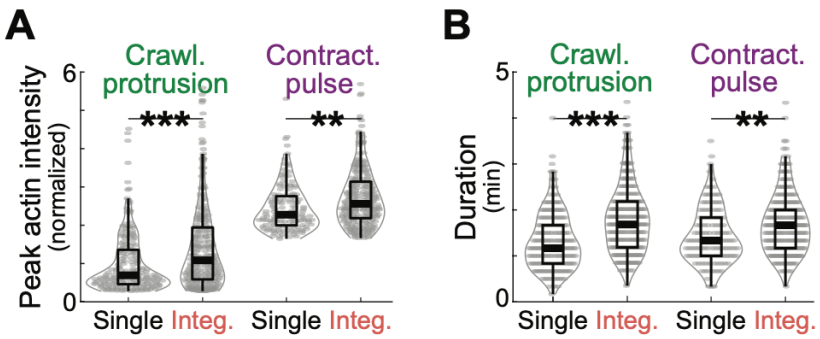

Figure 5. A novel vertex model provides insights into the biomechanics of crawling, contraction, and adhesion during convergent extension. (A) Each individual cell was modelled as a 60-vertex polygon. (B) The model involves a "contraction" force between vertices, F_1, a crawling force protruding from ML vertices F_2, and a cadherin adhesion force F_3 holding cell together. (C) Example of intercalation of four cells using the model. (D) Example of intercalation of 22 cells using the model. (E, F) The model recapitulates enhanced intercalation displacement and higher velocity for integrated steps as compared to crawling or contraction alone. (G) Synergistic effect of integration on protrusion duration observed *in vivo* (see Fig. 4B, green) is recapitulated in the model when crawling forces are relatively low (left) and when contraction forces are relatively high (right). (H) Synergistic effect of integration on contraction force observed *in vivo* (see Fig. 4A, purple) is recapitulated in the model when crawling forces are relatively low (left) and when contraction forces are relatively high (right).

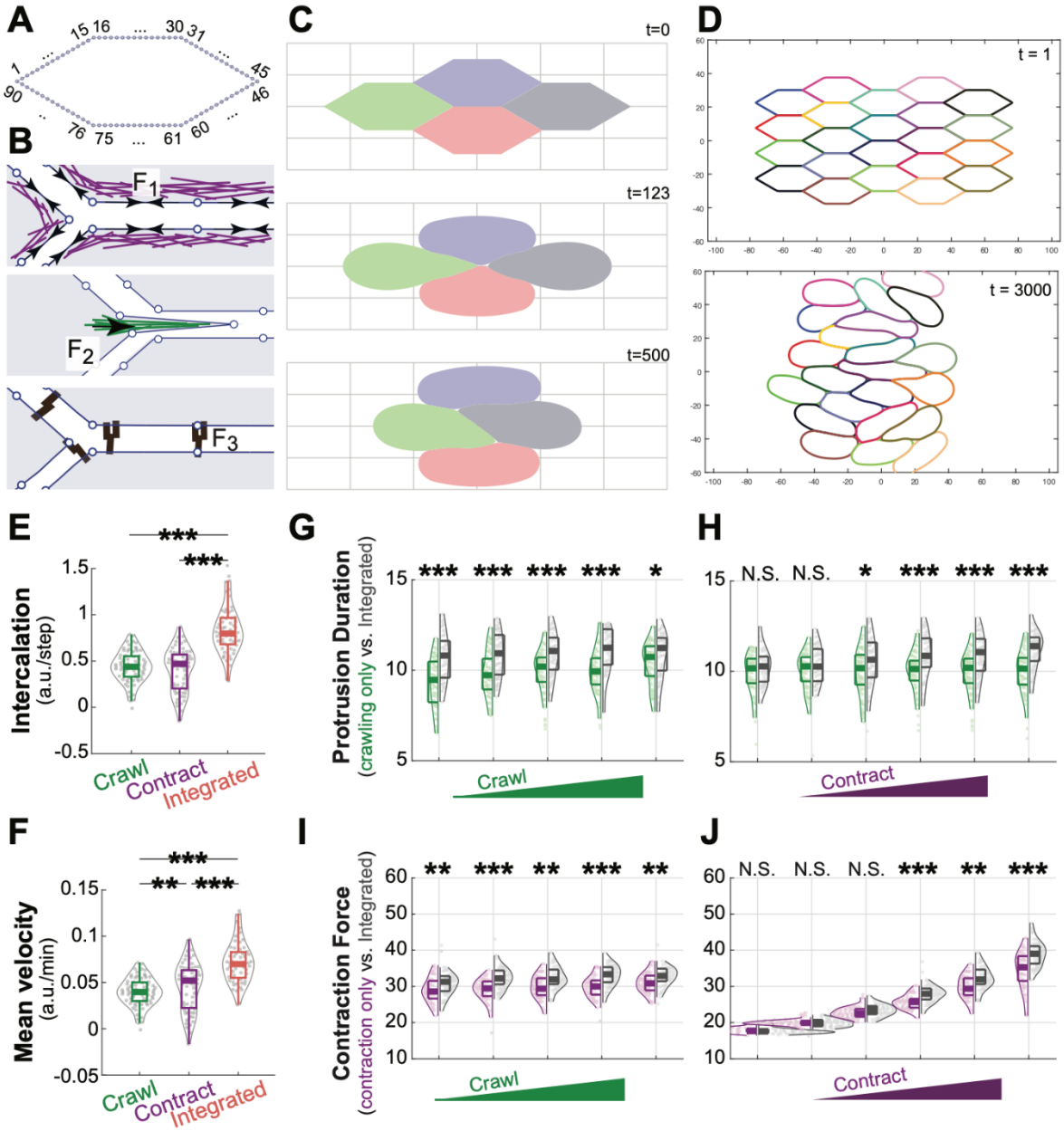

Figure 6. Cell adhesion is critical to integration of crawling and contraction. (A) Lower adhesion strongly favors crawling-only intercalation and suppresses contraction-only intercalation, however, improved intercalation of integrated steps in the model is robust to changes in cell adhesion. (B) Synergistic effect of integration on protrusion duration observed *in vivo* (see Fig. 4B, green) is improved in the model at relatively high levels of adhesion (left). (C) Synergistic effect of integration on contraction force observed *in vivo* (see Fig. 4A, purple) is improved in the model at lower adhesion levels.

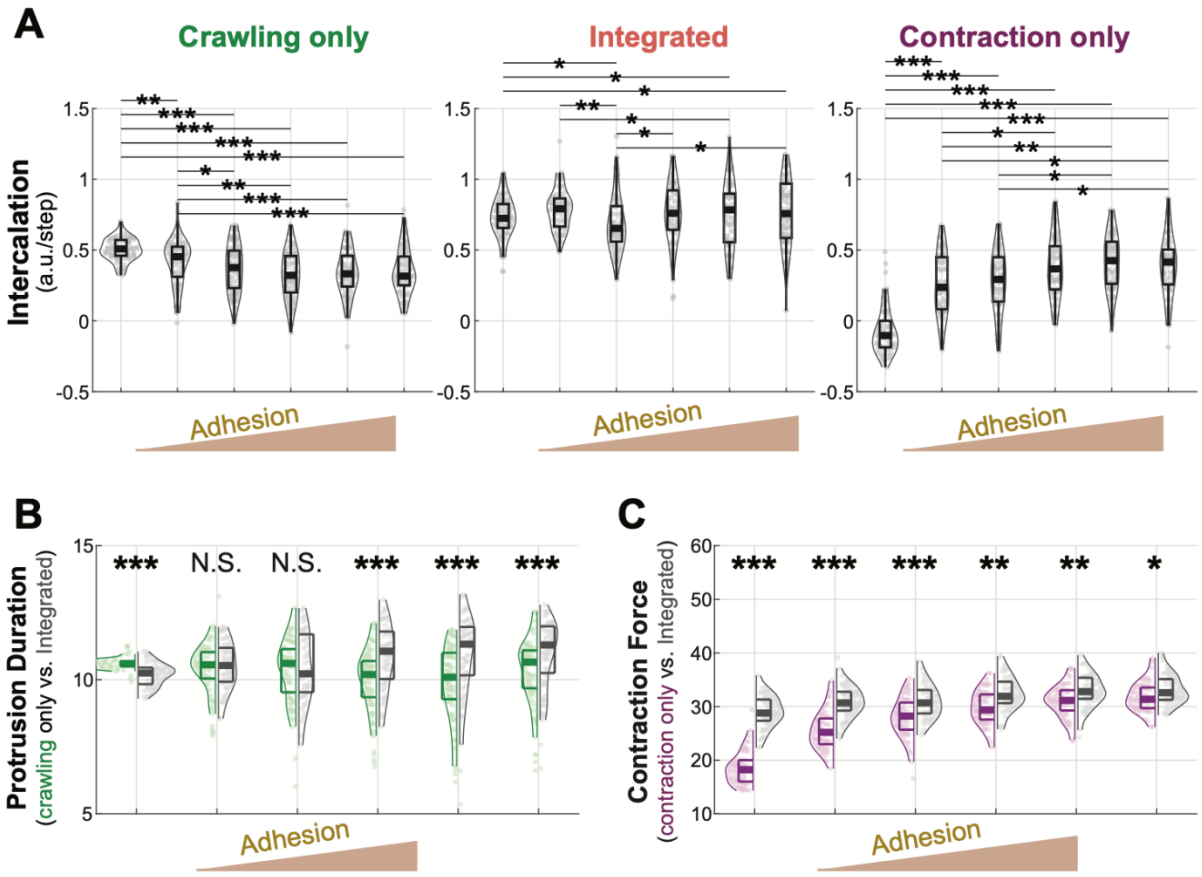

Figure 7. The ARVCF catenin is specifically required for integration of crawling and contraction. (A) Still images of membrane-GFP labelled cells in Keller explants, both control and Arvcf morphants display normal mediolateral polarization. (B). Overall intercalation velocity is significantly reduced by Arvcf knockdown. (C, D) Arvcf knockdown does not alter the relative numbers or duration of crawling, contraction, or integrated intercalation steps. (E) Arvcf strongly reduces the displacement driven by integrated steps (orange) and increases the displacement from crawling-only steps (green). (F) Synergistic effect of integration on protrusion duration is eliminated by Arvcf knockdown. (G) Synergistic effect of integration on the intensity of ML actin assembly is significantly reduced by Arvcf knockdown. (H, I) Synergistic effect of integration on contraction duration and intensity is unaffected by Arvcf knockdown.

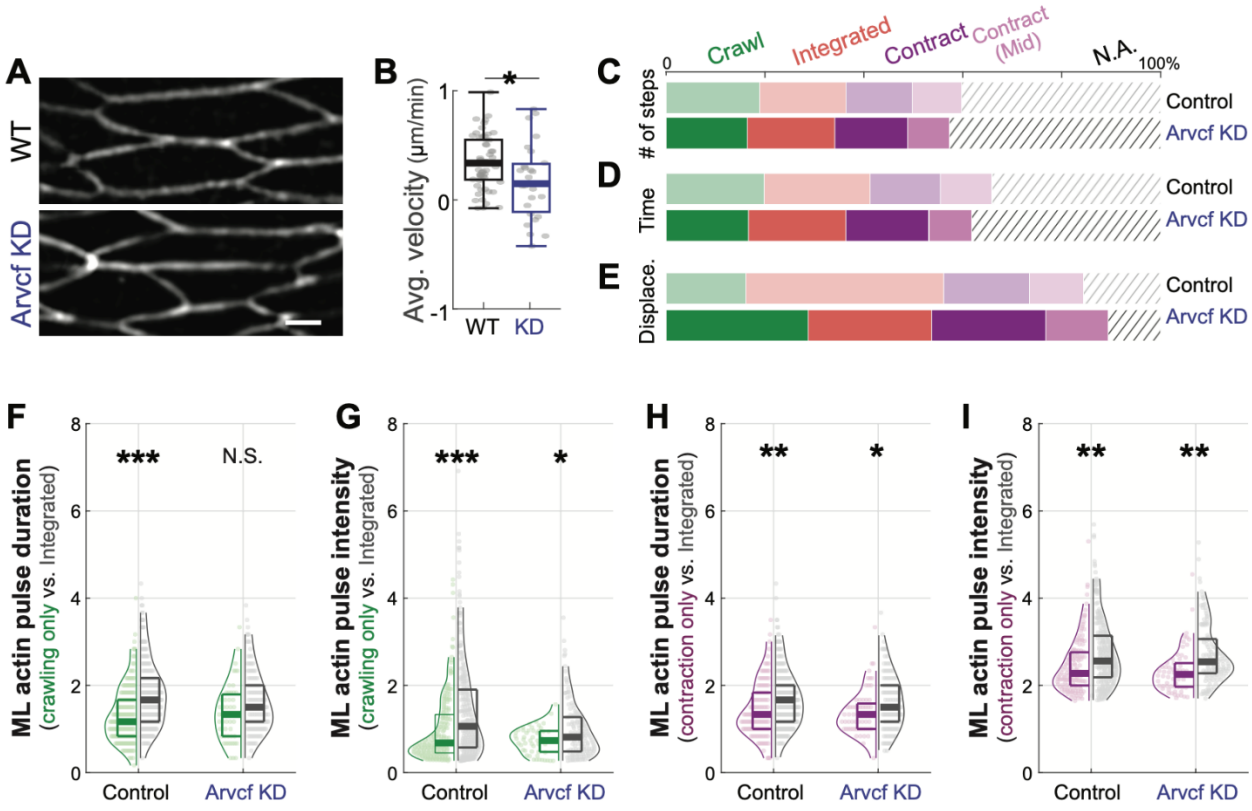

Acknowledgements:

This work was supported by grants from the NICHD (R01HD099191;1R21HD103882).

Methods:

***Xenopus* embryo manipulations:** Ovulation was induced by injecting adult female Xenopus laevis with 600 units of human chorionic gonadotropin (HCG, XXXXXXXXX) and animals were kept at 16 dc overnight. Eggs were acquired the following day by squeezing the ovulating females and eggs were fertilized *in vitro*. Eggs were dejellied in 2.5% cysteine (pH 8) 1.5 hours after fertilization and reared in 1/3x Marc's modified Ringer's (MMR) solution. For micro-injection, embryos were placed in 2% ficoll in 1/3x MMR during injection and washed in 1/3x MMR 30 min after injection. Embryos were injected in the dorsal blastomeres at the 4-cell stage targeting the C1 cell at 32-cell stage and presumptive notochord. Keller explants were dissected at stage 10.25 in Steinberg's solution using hair tools.

Plasmids and Morpholinos: The ARVCF morpholino has been previously described (5'-ACACTGGCAGACCTGAGCCTATGGC-3' (Fang et al., 2004)) and was ordered from Gene Tools, LLC. Lifeact-GFP and Lifeact-RFP were made in pCS and membrane-BFP in pCS2.

mRNA and morpholino microinjections: Capped mRNA was generated using the ThermoFisher SP6 mMessage mMachine kit (Catalog number: AM1340). mRNAs were injected at the following concentrations per blastomere: Mem-BFP (75 pg), Lifeact-RFP (75 pg), and Lifeact-GFP (75 pg). ARVCF morpholino was injected at a concentration of 10ng per blastomere.

Imaging *Xenopus* explants: Explants were submerged in Steinberg's solutions and cultured on glass coverslips coated with Fibronectin (Sigma-Aldrich, F1141) at 5 μg/cm^2. After 5-hour incubation at room temperature, we started standard confocal time-lapse imaging using a Nikon A1R. Images of membrane-BFP, Lifeact-GFP, and Lifeact-RFP were taken at a focal plane 5 μm deep into the explant and at an interval of 10 sec.

Cell segmentation: All image process and analysis were performed using customized MATLAB scripts if not mentioned otherwise. We first performed cell segmentation and junction detection on images of Mem-BFP. Briefly, we used pixel classification in ilastik (Berg et al., 2019), a machine-learning based open-resource image analysis tool, to classify pixels at cell-cell interface and pixels in cytoplasm. This process converted a time-lapse movie of fluorescence intensity images to a time-lapse movie of probability images, in which integrated information not only on pixel intensity but also gradient. We then extracted skeletons, where the probability peaks, of each probability image for a robust detection of cell-cell interfaces and cell segmentation.

Measurement of cell intercalation: We defined cell intercalation as the displacement of a tricellular vertex along the direction to shorten the AP interface (**Fig.S2A**). Each tricellular vertex was tracked over time on the segmented images and its displacement in the tangential direction of the AP interface ("in-plane") between adjacent timepoints was quantified. (**Fig.S2A**). This is the displacement component that contributes to cell intercalation and junction shortening. The transverse movement of a tricellular vertex leads to junction rotation and was neglected here.

Measurement of crawling and contraction signals: For the quantification of actin intensity, a 2 μm thick band along the AP junction was extracted. Regional actin dynamics was quantified by dividing such bands into tCRs and the middle regions. The tCRs have a minimum of 4 μm in length and covered the entire protrusions from the mediolateral cells if there were any. The middle regions were complementary to the tCRs and had a minimum length of 2 μm (**Fig. S2B.a2&3**). The raw crawling and contraction signals for cell intercalation were the average actin fluorescent intensity in the correspondence tCRs, if not otherwise specified (**Fig.S2B.a5**).

Normalization of fluorescence intensity signals: To allow for comparison of fluorescence intensity from different cells and different actin biosensors, we normalized the fluorescence intensity of each cell with its mean cytosolic background intensity. Briefly, we used cell segmentation mentioned earlier to generate a cytosolic mask for each cell which excluded cell-cell interface and cell cortex with a 3 μm margin (**Fig. S2B.a1**). The mean fluorescence intensity within each cytosolic mask was quantified and its moving average over 6 min was calculated and used for normalization (**Fig. S2B.a4-6**).

Kymograph preparation: We customized the preparation of kymograph so that it not only displays actin fluorescence intensity values from crawling (ML cells) or contraction (AP) signals but also displays the movement of tricellular vertices explicitly. Briefly, we extracted 2 μm thick bands along the AP junction from images of actin labeling, linearized the bands, calculated the normalized mean fluorescence intensity across the thickness, then stacked data from each timepoint along the time axis. For a direct display of tricellular vertex movement, we used in-plane displacement at each time point as a reference to align the kymograph.

Vertex model to simulate convergent extension: To study how crawling and contraction act in concert to drive convergent extension, we designed a novel CE model that offers a detailed description of subcellular behaviors of the cells and allows for cells take an arbitrary shape under subcellular forces. Each cell is represented by a 90-vertex polygon that is initially a hexagon and connects to its neighboring cells via cell-cell adhesion.

The dynamics of the model is driven by simple Newtonian mechanics with the basic assumption that vertices are embedded in viscous medium that applies a viscous dragging force with the damping parameter η and inertia vanishes. This leads to the governing equation for the evolution of the position $\boldsymbol{x_i}$ of vertex i determined by

$$\eta \frac{d\boldsymbol{x}i}{dt} = \boldsymbol{F_i}$$

where $\boldsymbol{F_i}$ is the total force acting on the vertex. Each simulation step is run by determining the forces acting on each vertex and solving the system of first-order differential equations using two-step Adam-Bashforth method with timestep $\Delta t = 0.1$. Vertices for each cell were reset every 10 steps to homogenize the edge length and avoid over-crowding of the vertices within regions of high contraction.

We considered three key force components in our model for the study of crawling and contraction: (1) contractile force on cell edges simulating contraction at cell cortex, (2) pushing force on the “leading” edge simulating lamellipodia and filopodia-like protrusions, and (3) adhesive force between cells simulating cadherin dependent cell adhesion. Secondary force components incorporated into our models include (4) elastic cytosolic pressure maintaining the area of a cell and (5) repulsive force between cells to avoid cell collision, and the parameters associated with them are all fixed in this study. Without loss of generosity, this model is a

dimensionless one, but parameters for the key force components are estimated from experimental data, which mains their relative values in a physiological relevant range (Table.1).

Contraction at cell cortex.

Contraction on the edge of a cell is modeled as pieces of Hill's muscle connected in series. The contractile force between two neighboring vertices equals:

$$F_m = \begin{cases} M \cdot f_{stall} \cdot (1 - \dot{\varepsilon}/\dot{\varepsilon_o}), & \dot{\varepsilon} < 0 \\ M \cdot f_{stall}, & \dot{\varepsilon} \geq 0 \end{cases}$$

where M is the polarity-dependent density of actomyosin, f_{stall} is the stall force, $\dot{\varepsilon}$ is the strain rate of the edge defined by the vertices, and $\dot{\varepsilon_o}$ is the maximum contractile strain rate when force vanishes. To simulate local actomyosin pulses at the AP interface, extra M, M_{pulse} is added to tricellular regions or the middle of the AP interface for a period of T_m as a half-sine pulse.

Pushing force for cell crawling and protrusion extension.

We assumed two different forces associated with cell crawling, one for lamellipodia-like pushing on the "leading" edge and one for filopodia-like pushing on a more restricted area. The direction of cell crawling is first defined in a polarity-pendent manner and lasts for T_l. A small pushing force F_l is applied to all vertices on the "leading" edge. Filopodia-like protrusions form stochastically on vertices that meet both requirements (1): in tri-cellular regions and (2) on the "leading" edge. When a protrusion is initiated, a quartile-sine force pulse with that maximum at F_p and the duration of T_p is applied to the vertex in the direction toward the interface between its two neighboring cells. For our analysis highlighting the integration between protrusions and contraction, F_l itself does not make cells intercalate.

Cell-cell adhesion and force transmission.

Cell-cell adhesion is based on cadherin clustering via its trans- and cis- interaction and force transmission via cadherin clusters and cadherin-catenin complex binding to the actomyosin network. Although the dynamics of cadherin clustering and cadherin-catenin binding to actin both depend on force, the latter is indictive of a catch bond with the transition force much smaller than the force range of interest for cadherin clustering (Buckley et al., 2014b; Rakshit et al., 2012). Therefore, we believe cadherin-catenin binding to actin is the limiting factor and we modeled adhesion cluster as a catch-bond cluster (Novikova and Storm, 2013).

For a single catch-bond, the force dependent unbinding rate can be expressed as $k_u(f) = k_0 \cdot [exp(-f/f^* + \phi_c) + \exp(f/f^* - \phi_s)]$, where k_0 is a reference unbinding rate and set to 1 s^{-1}, f is the force on the bond, f^* is a force scale used to non-dimensionalize all forces, and ϕ_c and ϕ_s represent zero-force unbinding rates associated with the catch and slip portion of the bond dynamics, respectively. Considering an adhesion cluster of the size N and the tensile load F_a is uniformly distributed on all bonds, the temporal evolution of the cluster size is expressed as

$$\frac{dN}{dt} = \gamma \cdot k_0 \cdot (N_{adhesion} - N) - k_0 \cdot \left[exp\left(-\frac{F_a}{N \cdot f^*} + \phi_c\right) + exp(\frac{F_a}{N \cdot f^*} - \phi_s)\right]$$

where γ is a dimensionless rebinding rate and $N_{adhesion}$ is the total adhesion units available in the vicinity. Under a quasistatic state, N and F_A can reach their maximum given by $N_{max} =$

$\frac{\alpha\gamma}{\alpha\gamma+2}N_{adhesion}$ and $F_{amax} = N_{max} \cdot \phi_{max} \cdot f^*$, where $\alpha = exp\,(\phi_s/2 - \phi_c/2)$ and $\phi_{max} = (\phi_s + \phi_{c)}/2$ (see detailed deduction in (Novikova and Storm, 2013).

Clustering is designed to initiate between any edge-vertex pairs from two neighboring cells when the distance between them, d is larger than d_r, a repulsion limit defined later to avoid cell collision, but smaller than d_a, the adhesion limit. The two anchoring points move with the vertices around them and are allowed to sit anywhere on cell edges.

The adhesive force applied via an adhesion cluster is estimated by $F_{a-e} = k_a \cdot N \cdot (d - d_r)$, where k_a is the unit spring constant and d is the distance between the two anchoring points of a cluster. k_a is estimated assuming a cluster under a slowly increasing tension reaches its maximum size of N_{max} and maximum load of F_{amax} at d_a, and it is given by $k_a = f^*\phi_{max}/d_a$.

Cytosolic pressure

Cytoplasm is assumed to be linearly elastic, so the difference between the current cell area A and the rest area A_r provides a pressure on cell boundary to maintain the cell size. The cytoplasm potential energy is given by $E_c = \frac{1}{2}\, k_c \left(\frac{A-A_r}{A_r}\right)$, where k_c is the cytoplasm stiffness, and the force on each vertex i can be expressed as

$$F_i = \nabla_i E_c = -k_C \frac{A - A_0}{A_0} \langle y_{i-1} - y_{i+1}, x_{i+1} - x_{i-1} \rangle$$

Contact repulsion

Repulsive forces are applied to any vertex-edge pairs from two neighboring cells if the distance between them d if less than d_r or even the vertex is inside the neighboring cell ($d < 0$). The magnitude of this repulsive force is an exponential function of d and is given by

$$F_r = F_{rmax} - (F_{rmax} - F_{r0}) \cdot \exp\,(\frac{d}{d_r} ln \frac{F_{rmax}}{F_{rmax} - F_{r0}})$$

where F_{r0} is the repulsion at $d = 0$, and F_{rmax} is the maximum repulsion if the vertex is inside a neighboring cell.

Table 1. Parameters for the vertex model

Parameter			Value	Reference
Iteration	Viscosity	η	20	-
	Timestep	Δt	0.1	-
Contraction	Stall force	f_{stall}	3	(Mitrossilis et al., 2009b)
	Actomyosin density	M	1 (ML) 2 (AP)	(Mitrossilis et al., 2009a)
		M_{pulse}	2-7	
	Min. strain rate	$\dot{\varepsilon_o}$	0.8	(Mitrossilis et al., 2009a)
Protrusion	Lamellipodia force	F_l	0.5	-
	Lamellipodia duration	T_l	100	-
	Protrusion force	F_p	14-18	(Abraham et al., 1999; Prass et al., 2006)
	Protrusion duration	T_p	6	-
Adhesion	Force scale	f^*	0.005	(Buckley et al., 2014a)
	Catch unbinding rate	ϕ_c	1.0322	(Buckley et al., 2014a)
	Slip unbinding rate	ϕ_s	2.9671	(Buckley et al., 2014b)
	Rebinding rate	γ	2	-
	Total available bond	N_t	200-1200	(Truong Quang et al., 2013)
	Adhesion range	d_a	0.25	-
Cytoplasm	Rest area/Initial area	A_r/A_0	1.004	(Petrie et al., 2014b)
	Stiffness	k_C	100	(Petrie et al., 2014a)
Repulsion	Maximum force	F_{rmax}	4	-
	Force at zero distance	F_{r0}	1	-
	Repulsion range	d_r	0.025	-

References:

Abraham, V.C., V. Krishnamurthi, D.L. Taylor, and F. Lanni. 1999. The actin-based nanomachine at the leading edge of migrating cells. *Biophys J*. 77:1721-1732.

Alt, S., P. Ganguly, and G. Salbreux. 2017. Vertex models: from cell mechanics to tissue morphogenesis. *Philos Trans R Soc Lond B Biol Sci*. 372.

Berg, S., D. Kutra, T. Kroeger, C.N. Straehle, B.X. Kausler, C. Haubold, M. Schiegg, J. Ales, T. Beier, M. Rudy, K. Eren, J.I. Cervantes, B. Xu, F. Beuttenmueller, A. Wolny, C. Zhang, U. Koethe, F.A. Hamprecht, and A. Kreshuk. 2019. ilastik: interactive machine learning for (bio)image analysis. *Nat Methods*. 16:1226-1232.

Bertet, C., L. Sulak, and T. Lecuit. 2004. Myosin-dependent junction remodelling controls planar cell intercalation and axis elongation. *Nature*. 429:667-671.

Brieher, W.M., and B.M. Gumbiner. 1994. Regulation of C-cadherin function during activin induced morphogenesis of Xenopus animal caps. *J Cell Biol*. 126:519-527.

Buckley, C.D., J. Tan, K.L. Anderson, D. Hanein, N. Volkmann, W.I. Weis, W.J. Nelson, and A.R. Dunn. 2014a. Cell adhesion. The minimal cadherin-catenin complex binds to actin filaments under force. *Science*. 346:1254211.

Buckley, C.D., J. Tan, K.L. Anderson, D. Hanein, N. Volkmann, W.I. Weis, W.J. Nelson, and A.R. Dunn. 2014b. The minimal cadherin-catenin complex binds to actin filaments under force. *Science*. 346:1254211.

Butler, M.T., and J.B. Wallingford. 2017. Planar cell polarity in development and disease. *Nat Rev Mol Cell Biol*. 18:375-388.

Cho, K., M. Lee, D. Gu, W.A. Munoz, H. Ji, M. Kloc, and P.D. McCrea. 2011. Kazrin, and its binding partners ARVCF- and delta-catenin, are required for Xenopus laevis craniofacial development. *Dev Dyn*. 240:2601-2612.

Cho, K., T.G. Vaught, H. Ji, D. Gu, C. Papasakelariou-Yared, N. Horstmann, J.M. Jennings, M. Lee, L.M. Sevilla, M. Kloc, A.B. Reynolds, F.M. Watt, R.G. Brennan, A.P. Kowalczyk, and P.D. McCrea. 2010. Xenopus Kazrin interacts with ARVCF-catenin, spectrin and p190B RhoGAP, and modulates RhoA activity and epithelial integrity. *J Cell Sci*. 123:4128-4144.

Chu, C.W., G. Masak, J. Yang, and L.A. Davidson. 2020. From biomechanics to mechanobiology: Xenopus provides direct access to the physical principles that shape the embryo. *Curr Opin Genet Dev*. 63:71-77.

Fagotto, F., N. Rohani, A.S. Touret, and R. Li. 2013. A molecular base for cell sorting at embryonic boundaries: contact inhibition of cadherin adhesion by ephrin/ Eph-dependent contractility. *Dev Cell*. 27:72-87.

Fang, X., H. Ji, S.W. Kim, J.I. Park, T.G. Vaught, P.Z. Anastasiadis, M. Ciesiolka, and P.D. McCrea. 2004. Vertebrate development requires ARVCF and p120 catenins and their interplay with RhoA and Rac. *J Cell Biol*. 165:87-98.

Fernandez-Gonzalez, R., M. Simoes Sde, J.C. Roper, S. Eaton, and J.A. Zallen. 2009. Myosin II dynamics are regulated by tension in intercalating cells. *Dev Cell*. 17:736-743.

Fletcher, A.G., F. Cooper, and R.E. Baker. 2017. Mechanocellular models of epithelial morphogenesis. *Philos Trans R Soc Lond B Biol Sci*. 372.

Goto, T., and R. Keller. 2002. The planar cell polarity gene strabismus regulates convergence and extension and neural fold closure in Xenopus. *Dev Biol*. 247:165-181.

Huebner, R., A.N. Malmi-Kakkada, S. Sarikaya, S. Weng, D. Thirumalai, and J.B. Wallingford. 2020. Mechanical heterogeneity along single cell-cell junctions is driven by lateral clustering of cadherins during vertebrate axis elongation. *bioRxiv*.

Huebner, R.J., and J.B. Wallingford. 2018. Coming to Consensus: A Unifying Model Emerges for Convergent Extension. *Dev Cell*. 46:389-396.

Keller, R., L.A. Davidson, and D.R. Shook. 2003. How we are shaped: the biomechanics of gastrulation. *Differentiation*. 71:171-205.

Keller, R., and J. Hardin. 1987. Cell behaviour during active cell rearrangement: evidence and speculations. *J Cell Sci Suppl*. 8:369-393.

Keller, R., and P. Tibbetts. 1989. Mediolateral cell intercalation in the dorsal, axial mesoderm of Xenopus laevis. *Dev Biol*. 131:539-549.

Kim, H.Y., and L.A. Davidson. 2011. Punctuated actin contractions during convergent extension and their permissive regulation by the non-canonical Wnt-signaling pathway. *J Cell Sci*. 124:635-646.

Kinoshita, N., H. Iioka, A. Miyakoshi, and N. Ueno. 2003. PKC delta is essential for Dishevelled function in a noncanonical Wnt pathway that regulates Xenopus convergent extension movements. *Genes Dev*. 17:1663-1676.

Levayer, R., and T. Lecuit. 2013. Oscillation and polarity of E-cadherin asymmetries control actomyosin flow patterns during morphogenesis. *Dev Cell*. 26:162-175.

Lienkamp, S.S., K. Liu, C.M. Karner, T.J. Carroll, O. Ronneberger, J.B. Wallingford, and G. Walz. 2012. Vertebrate kidney tubules elongate using a planar cell polarity-dependent, rosette-based mechanism of convergent extension. *Nat Genet*. 44:1382-1387.

Martin, A.C., M. Gelbart, R. Fernandez-Gonzalez, M. Kaschube, and E.F. Wieschaus. 2010. Integration of contractile forces during tissue invagination. *J Cell Biol*. 188:735-749.

McCrea, P.D., and J.I. Park. 2007. Developmental functions of the P120-catenin sub-family. *Biochim Biophys Acta*. 1773:17-33.

Merkel, M., and M.L. Manning. 2017. Using cell deformation and motion to predict forces and collective behavior in morphogenesis. *Semin Cell Dev Biol*. 67:161-169.

Mitrossilis, D., J. Fouchard, A. Guiroy, N. Desprat, N. Rodriguez, B. Fabry, and A. Asnacios. 2009a. Single-cell response to stiffness exhibits muscle-like behavior. *Proceedings of the National Academy of Sciences*. 106:18243-18248.

Mitrossilis, D., J. Fouchard, A. Guiroy, N. Desprat, N. Rodriguez, B. Fabry, and A. Asnacios. 2009b. Single-cell response to stiffness exhibits muscle-like behavior. *Proc Natl Acad Sci U S A*. 106:18243-18248.

Nishimura, T., H. Honda, and M. Takeichi. 2012. Planar cell polarity links axes of spatial dynamics in neural-tube closure. *Cell*. 149:1084-1097.

Novikova, E.A., and C. Storm. 2013. Contractile fibers and catch-bond clusters: a biological force sensor? *Biophys J*. 105:1336-1345.

Petrie, R.J., H. Koo, and K.M. Yamada. 2014a. Generation of compartmentalized pressure by a nuclear piston governs cell motility in a 3D matrix. *Science*. 345:1062.

Petrie, R.J., H. Koo, and K.M. Yamada. 2014b. Generation of compartmentalized pressure by a nuclear piston governs cell motility in a 3D matrix. *Science*. 345:1062-1065.

Pfister, K., D.R. Shook, C. Chang, R. Keller, and P. Skoglund. 2016. Molecular model for force production and transmission during vertebrate gastrulation. *Development*. 143:715-727.

Prass, M., K. Jacobson, A. Mogilner, and M. Radmacher. 2006. Direct measurement of the lamellipodial protrusive force in a migrating cell. *J Cell Biol*. 174:767-772.

Rakshit, S., Y. Zhang, K. Manibog, O. Shafraz, and S. Sivasankar. 2012. Ideal, catch, and slip bonds in cadherin adhesion. *Proceedings of the National Academy of Sciences*. 109:18815.

Rauzi, M., P. Verant, T. Lecuit, and P.F. Lenne. 2008. Nature and anisotropy of cortical forces orienting Drosophila tissue morphogenesis. *Nat Cell Biol*. 10:1401-1410.

Reintsch, W.E., C.A. Mandato, P.D. McCrea, and F. Fagotto. 2008. Inhibition of cell adhesion by xARVCF indicates a regulatory function at the plasma membrane. *Dev Dyn*. 237:2328-2341.

Shih, J., and R. Keller. 1992. Cell motility driving mediolateral intercalation in explants of Xenopus laevis. *Development*. 116:901-914.

Shindo, A. 2018. Models of convergent extension during morphogenesis. *Wiley Interdiscip Rev Dev Biol*. 7.

Shindo, A., Y. Inoue, M. Kinoshita, and J.B. Wallingford. 2019. PCP-dependent transcellular regulation of actomyosin oscillation facilitates convergent extension of vertebrate tissue. *Dev Biol*. 446:159-167.

Shindo, A., and J.B. Wallingford. 2014. PCP and septins compartmentalize cortical actomyosin to direct collective cell movement. *Science*. 343:649-652.

Sun, Z., C. Amourda, M. Shagirov, Y. Hara, T.E. Saunders, and Y. Toyama. 2017. Basolateral protrusion and apical contraction cooperatively drive Drosophila germ-band extension. *Nat Cell Biol*. 19:375-383.

Tada, M., and C.P. Heisenberg. 2012. Convergent extension: using collective cell migration and cell intercalation to shape embryos. *Development*. 139:3897-3904.

Tran, H.T., M. Delvaeye, V. Verschuere, E. Descamps, E. Crabbe, L. Van Hoorebeke, P. McCrea, D. Adriaens, F. Van Roy, and K. Vleminckx. 2011. ARVCF depletion cooperates with Tbx1 deficiency in the development of 22q11.2DS-like phenotypes in Xenopus. *Dev Dyn*. 240:2680-2687.

Truong Quang, B.A., M. Mani, O. Markova, T. Lecuit, and P.F. Lenne. 2013. Principles of E-cadherin supramolecular organization in vivo. *Curr Biol*. 23:2197-2207.

Wallingford, J.B., B.A. Rowning, K.M. Vogeli, U. Rothbacher, S.E. Fraser, and R.M. Harland. 2000. Dishevelled controls cell polarity during Xenopus gastrulation. *Nature*. 405:81-85.

Williams, M., W. Yen, X. Lu, and A. Sutherland. 2014. Distinct apical and basolateral mechanisms drive planar cell polarity-dependent convergent extension of the mouse neural plate. *Dev Cell*. 29:34-46.

Zallen, J.A., and E. Wieschaus. 2004. Patterned gene expression directs bipolar planar polarity in Drosophila. *Dev Cell*. 6:343-355.

Supp. Figure 1. Mosaic labeling of actin to distinguish crawling and contraction signals at cell interface. (A) Schematic illustrating mosaic expression of LifeAct-RFP and LifeAct-GFP. LifeAct-RFP and membrane-BFP mRNAs are injected into the left dorsal blastomere of 4-cell stage embryos, and LifeAct-GFP and membrane-BFP into the right dorsal blastomere. (B) Representative images showing mosaic labeling of neighboring cells. Asterisks mark the tCRs where actin in the AP cells and actin in the M/L cell are labeled with different biosensors. Scalebar, 10 μm.

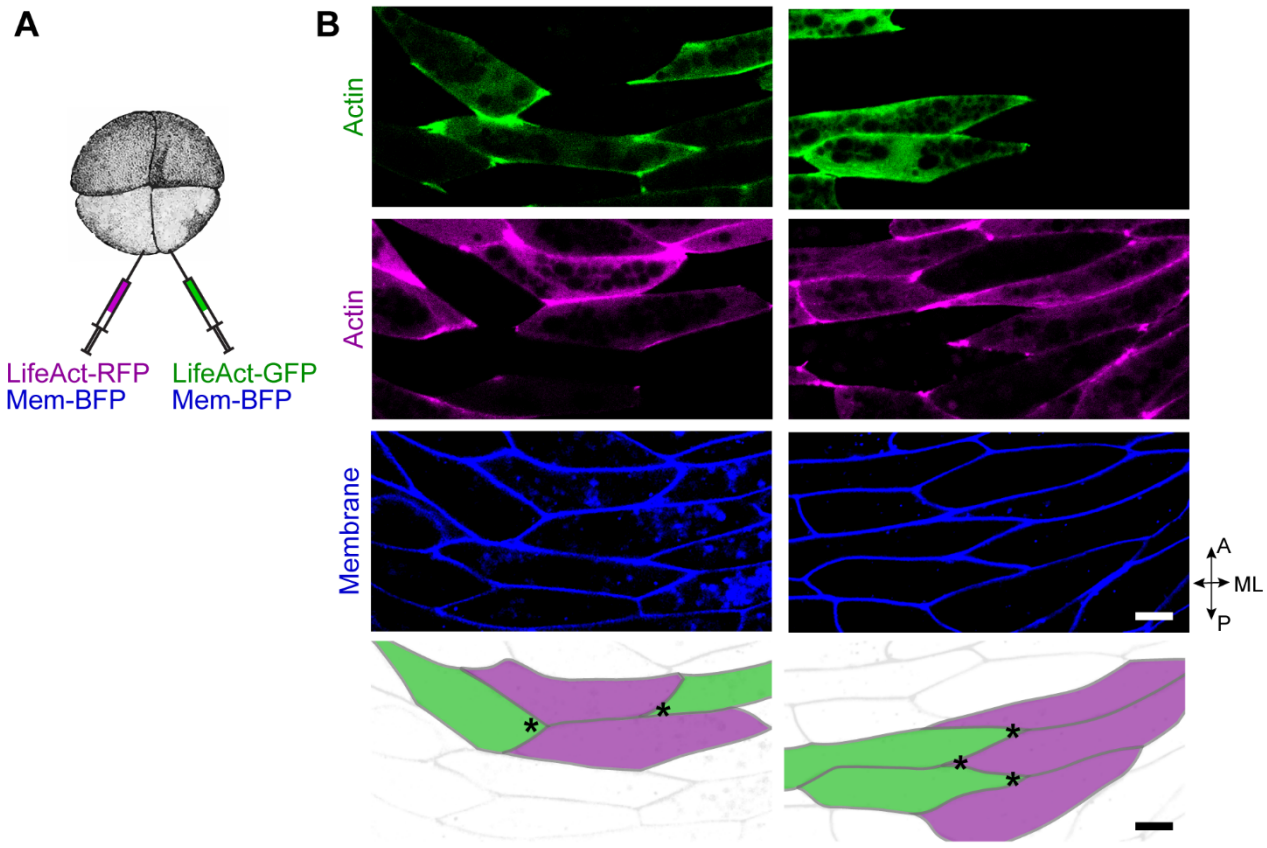

Supp. Figure 2. Image quantification. (A) Schematic illustrating the quantification of cell intercalation. Dashed blue lines and solid blue lines are the cell-cell interfaces at two adjacent time points. Black arrow shows the displacement vector of the tricellular vertex. Red arrow is the displacement along the AP interface at t_i (in-plane displacement), which contributes to cell intercalation. Gray arrow is the transverse displacement that does not contribute to cell intercalation. (B) Representative data illustrating fluorescence intensity normalization. (a1) Membrane labeling was used for segmentation (blue) and cytosolic masks were generated for the quantification of cytosolic fluorescence intensity (gray). (a2 & a3) Actin in the ML cells (a2) and in the AP cells (a3). Cell-cell interfaces were automatically detected using the membrane labeling (white dashed lines). tCRs where protrusions from the left (L) or right (R) cell colocalized with the AP interface were marked with white boxes. The middle region of the AP interface was also boxed for the quantification of contraction signal from the middle of the junction. (a4) Background cytosolic intensity of actin was defined as the mean actin intensity in a2 & a3 inside the regions marked with the cytosolic masks in a1 (solid lines). Their moving average over 6 min was taken and used for normalization (black dashed lines). (a5) The mean fluorescence intensity of actin in the boxed regions. (a6) Fluorescence intensity normalized by the moving average of background intensity.

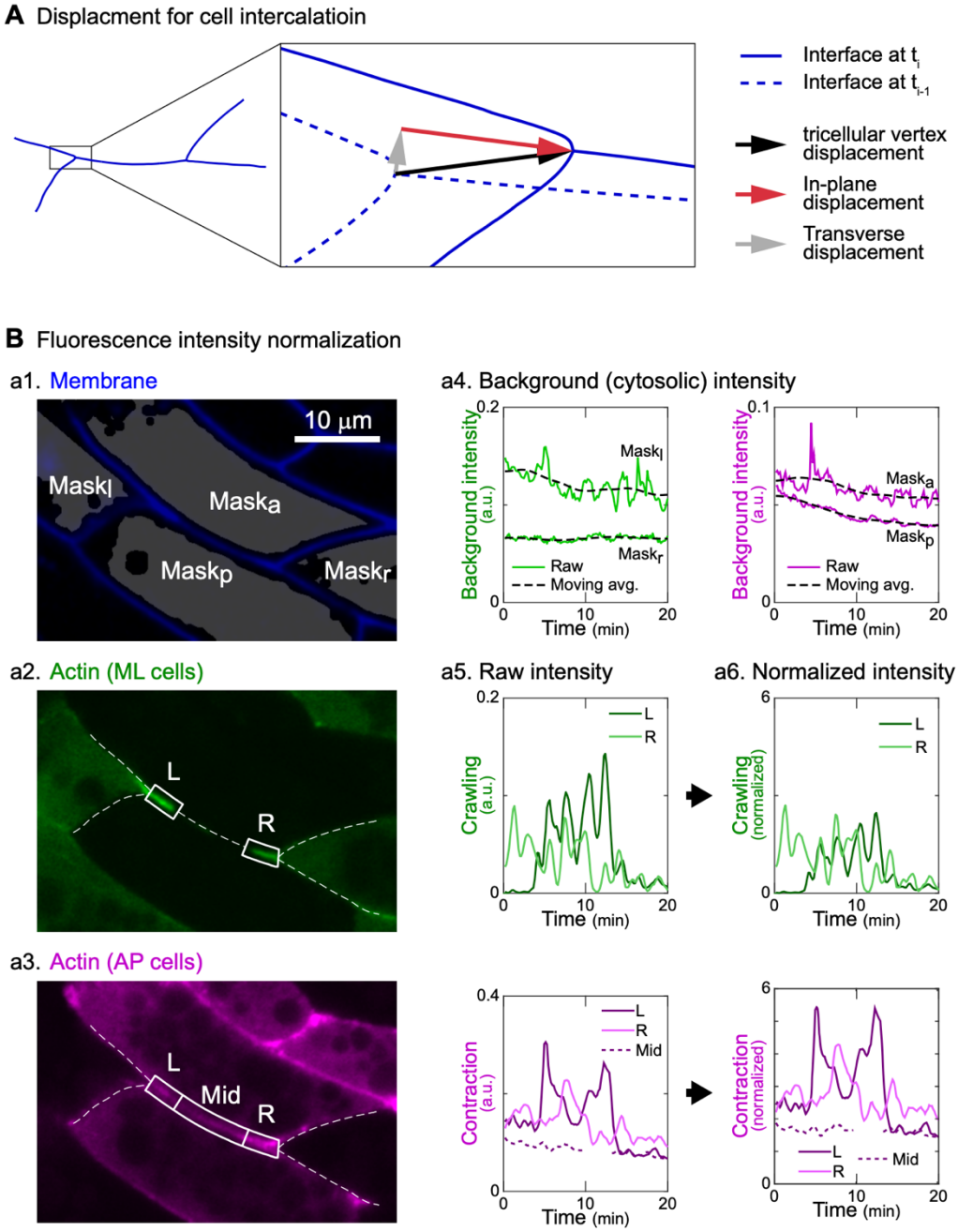

Supp. Figure 3. Cross-correlation between cell intercalation velocity, crawling signal, and contraction signal. (A) Cross correlation between cell intercalation velocity for paired tricellular vertices (left) and the distribution of the maximum cross correlation coefficient. n = 8. (B) Cross correlation between the contraction signal from the tCR and that from the middle of the junction (left) and the distribution of the maximum cross correlation coefficient (right). n = 50.. (C&D) Cell intercalation velocity of the left and right tricellular vertices in Fig.2A and the normalized crawling and contraction signals. (E-G) Cross-correlation between cell intercalation velocity, crawling signal, and contraction signal. Each line represents cell intercalation at one tCR. Solid lines, the left tCR in Fig.2A; dashed lines, the right tCR in Fig.2A; gray lines, all other tCRs in the data set. n = 57.

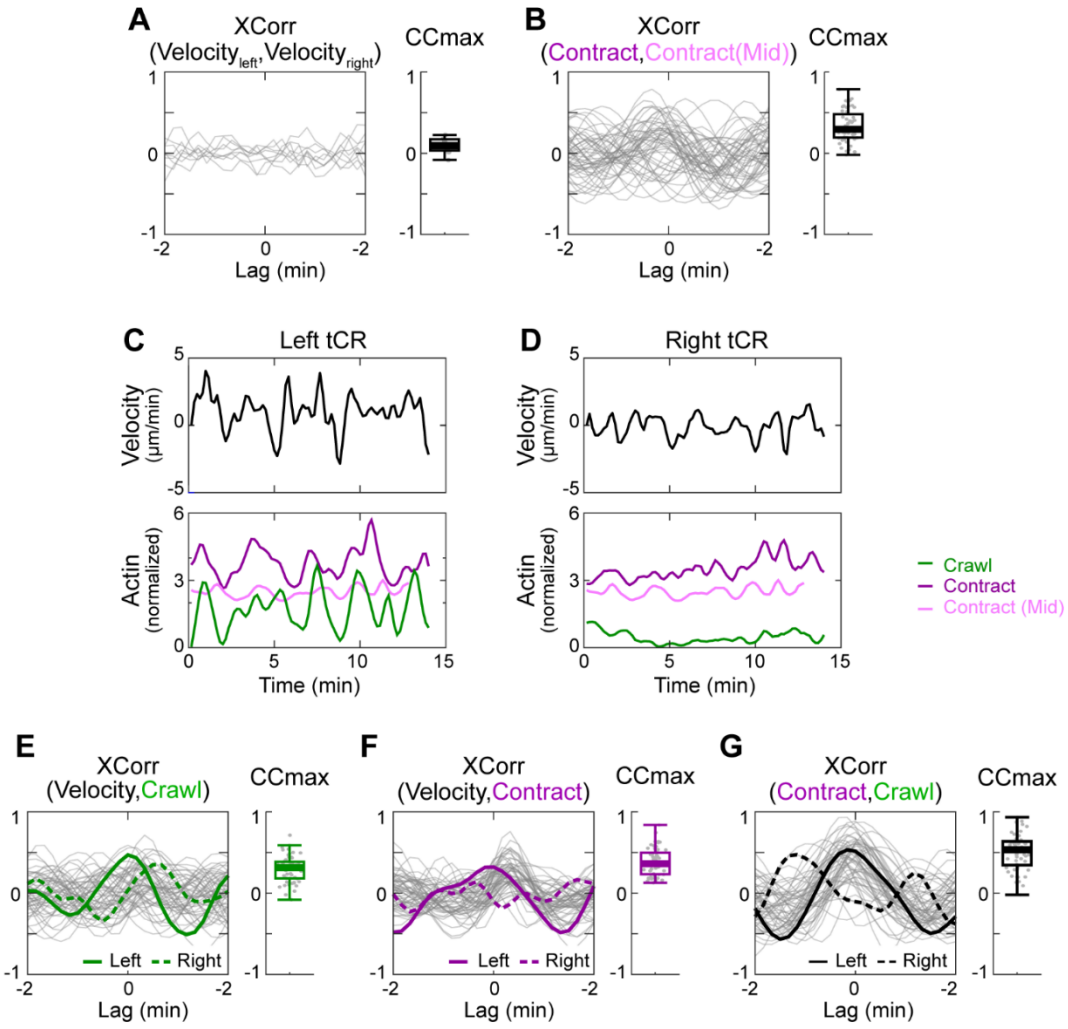

Supp. Figure 4. Classification of intercalation steps. (A) Intercalation step analysis for the tCRs in Fig. 2A. For each tCR, the intercalation velocity, crawling signal, contraction signal in the tCR, and the contraction from the middle of the AP interface were plotted verses time. Peaks and valleys were detected using customized scripts and individual peaks were separated with dashed lines at the adjacent valleys. An intercalation step was defined as an individual peak on the velocity curve and was classified based on its cross-correlation with pulses on the crawling and/or contraction curves. The correlated peaks were color-coded according to the figure legend. Intercalation steps that had no cross-correlation with crawling nor contraction pulses were filled with diagonal strips, while contraction and crawling pulses that had no cross-correlation with any intercalation step were filled with dots. Red arrows labelled correlated contraction and crawling pulses. Red double-line arrows marked correlated crawling and contraction pulses that are also correlated with different velocity peaks. Daggers marked continuous crawling-contraction integration where more than two crawling and contraction pulses were correlated sequentially. Letter b&c marked the timepoints for intercalation examples shown in (B-C). (B&C) Examples showing cell intercalation driven by another form of crawling- contraction integration where the contraction pulse precedes a crawling pulse (B) and by contraction from the middle of the AP interface (C).

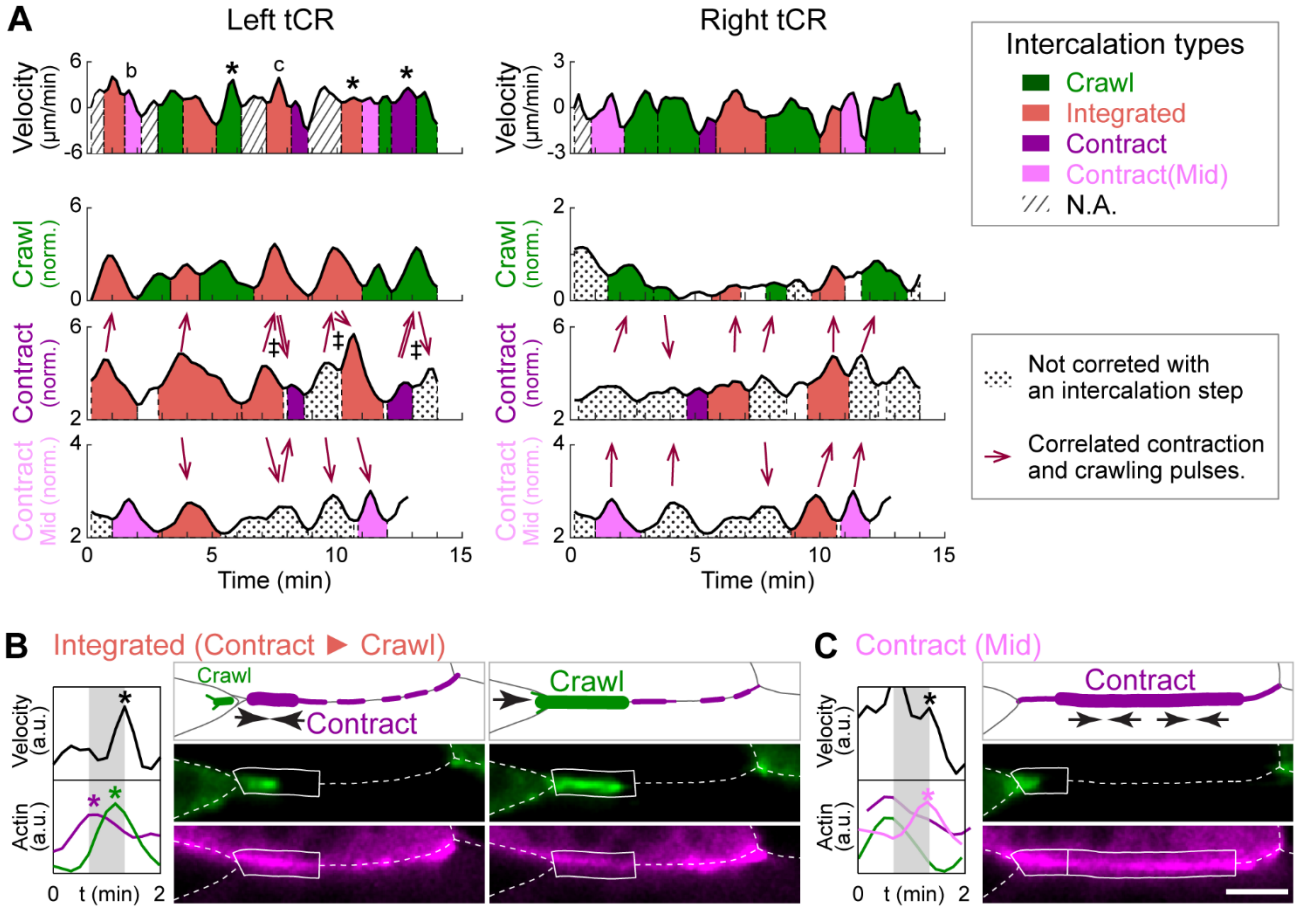

Supp. Figure 5. (A) Effect of increasing crawling force on intercalation (vertex displacement) during crawling, integrated, and contraction steps in the model. (B) Effect of increasing contraction on intercalation (vertex displacement) during crawling, integrated, and contraction steps in the model.